Energy loss of argon in a laser-generated carbon plasma

A. Frank,[1] A. Blažević,[2] P. L. Grande,[3] K. Harres,[1] T. Heßling,[2] D. H. H. Hoffmann,[1] R. Knobloch-Maas,[1] P. G. Kuznetsov,[4] F. Nürnberg,[1] A. Pelka,[1] G. Schaumann,[1] G. Schiwietz,[5] A. Schökel,[1] M. Schollmeier,[1] D. Schumacher,[1] J. Schütrumpf,[1] V. V. Vatulin,[4] O. A. Vinokurov,[4] and M. Roth[1]

[1]*Institut für Kernphysik, Technische Universität Darmstadt, Schlossgartenstraße 9, 64289 Darmstadt, Germany*

[2]*GSI Helmholtzzentrum für Schwerionenforschung GmbH, Planckstraße 1, 64291 Darmstadt, Germany*

[3]*Universidade Federal do Rio Grande do Sul, Avenida Bento Goncalves 9500, Porto Alegre 91501-970, RS, Brazil*

[4]*RFNC-VNIIEF, Sarov, Nizhny Novgorod Region 607190, Russia*

[5]*Helmholtz-Zentrum Berlin für Materialien und Energie, Glienicker Strasse 100, D-14109 Berlin, Germany*

(Received 16 December 2008; revised manuscript received 4 November 2009; published 4 February 2010)

The experimental data presented in this paper address the energy loss determination for argon at 4 MeV/u projectile energy in laser-generated carbon plasma covering a huge parameter range in density and temperature. Furthermore, a consistent theoretical description of the projectile charge state evolution via a Monte Carlo code is combined with an improved version of the CasP code that allows us to calculate the contributions to the stopping power of bound and free electrons for each projectile charge state. This approach gets rid of any effective charge description of the stopping power. Comparison of experimental data and theoretical results allows us to judge the influence of different plasma parameters.

DOI: 10.1103/PhysRevE.81.026401 PACS number(s): 52.20.Hv, 34.50.Bw, 52.40.Mj, 52.58.Hm

I. INTRODUCTION

The stopping power of heavy ions in matter is a field of research that has been addressed for about a century. From the pioneering works of Bohr [1], Bethe [2], and Bloch [3] to a lot more advanced and complete treatments such as in [4–6] the understanding of the interaction of charged particles with cold matter has continuously evolved and agrees rather well with experimental data [7] by now. However, the interaction of charged particles with ionized matter is not yet fully understood and there are only few experimental data to survey existing stopping power theories. The understanding of this stopping regime is of crucial importance to a variety of fields in physics, e.g., the realization of an ion-driven fast ignition concept [8,9] or the target response in modern accelerators such as the large hadron collider (LHC) or the facility for antiproton and ion research (FAIR) project. In the last two decades several experiments concerning the energy loss in plasma have been conducted covering the field of low-density plasma with an intermediate temperature of several eV produced by a gas discharge [10,11] to laser-generated plasma [12] with temperatures up to 60 eV as well as accessing the warm dense matter regime via heavy-ion heating [13] or shock waves [14].

The unique combination of the universal linear accelerator (UNILAC) with the high-energy laser for ion-beam experiments (nhelix) [15] allows the investigation of the interaction of heavy-ion beams with hot laser-generated plasma. This paper hence addresses experimental data of heavy-ion energy loss in carbon at higher temperatures and densities than in former experiments [11,12], reaching temperatures of up to 250 eV and densities covering the regime of a cold gas of several mbar up to a pressure of 70 bar. Very accurate results for the energy loss of argon at an energy of 4 MeV/u in carbon plasma are presented. At this projectile energy both projectile screening effects as well as changes in the excitation energies of bound and free electrons of the target play an important role. To quantify these effects the changes in the former parameter are calculated via a specially developed Monte Carlo (MC) code which determines the changes in the projectile charge state distribution in the carbon plasma. The stopping cross section for each argon charge state is calculated by a modified version of the CASP code [16], which allows us to calculate the contributions to the stopping power of free and bound electrons of the ionized carbon target as well. This approach does not use any effective charge description of the projectile in the plasma as, for example, the commonly used modification of the Bethe formula.

II. EXPERIMENTAL SETUP AND DATA

The energy loss is measured via the time-of-flight (ToF) method as shown in Fig. 1. Laser and ion beam—in this case $^{36}Ar^{16+}$ at 4 MeV/u—penetrate the target from opposite sides. The UNILAC accelerator delivers an ion beam with a length of 40 μs. This beam includes a substructure of 108 MHz, which permits us to probe the target every 9.224 ns. Each of these ion bunches has a Gaussian shape with a pulse width of 2–3 ns [full width at half-maximum (FWHM)]. As the ToF detector a chemical-vapor deposition (CVD) diamond detector has been developed which offers an increased

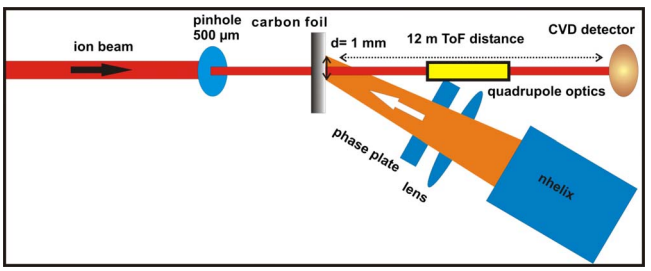

FIG. 1. (Color online) Experimental setup of the energy-loss measurements.

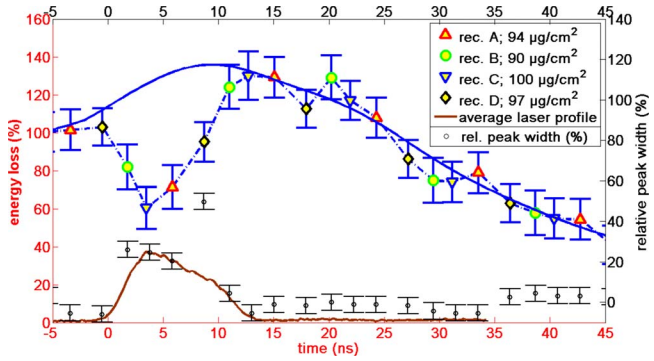

FIG. 2. (Color online) Experimental results for the energy loss of argon in carbon. For negative times the ion beam passes through the cold foil; for positive times the nhelix laser heats the target to the plasma state. The average temporal profile of the laser pulse is shown at the bottom. The relative peak width (0% corresponds to the ion pulse width in the cold foil) is also plotted in this picture. The upper solid blue line is the smoothed sum of the scaled laser pulse and the energy-loss values.

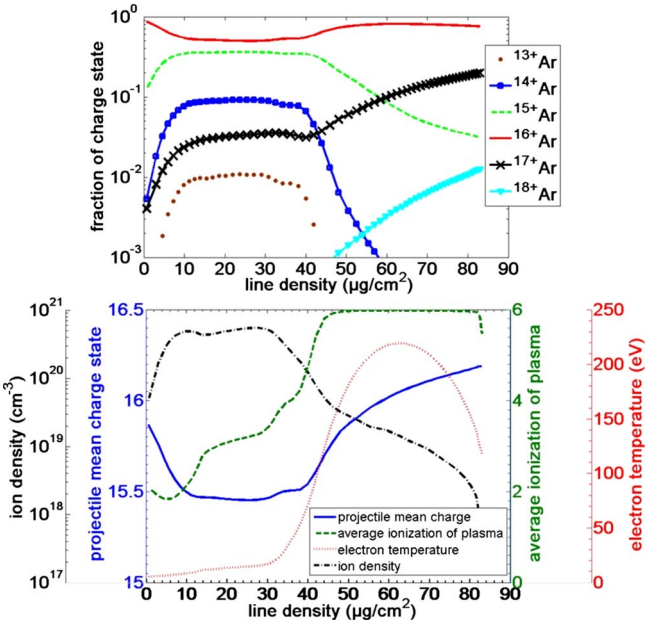

FIG. 3. (Color online) In the upper graph the calculated argon charge state distribution evolution in carbon plasma 12 ns after the beginning of the laser pulse is plotted. The lower graph shows the evolution of the corresponding projectile mean charge state. In addition, the plasma parameters derived by MIMOZA-2D simulations are shown in this graph. The line density $l(x)$ corresponds to $l(x)=\int_0^x x\rho(x')dx'$. The laser beam penetrates the target from the right; the Ar^{16+} beam penetrates from the left.

sensitivity due to a much shorter dead time compared to former multi chanel plate (MCP) or multisphere plate (MSP) detectors [12] at the given ion-beam intensities. Therefore, the ion-beam diameter could be reduced to 500 μm via a pinhole while the focus diameter of the nhelix heating pulse has been set to 1 mm. In addition, a random-phase plate has been used to smooth the spatial focus profile, so that the center of the plasma appears homogeneous for the ion beam. The nhelix laser system delivers laser pulses with an energy of 50 J and a pulse length of 10 ns (FWHM) at $\lambda = 1.064$ μm, which corresponds to a maximum intensity of 5×10^{11} W/cm^2 on the target.

To analyze the data the convolution of the detector response function and the Gaussian shape of the ion bunch is fitted to each detector signal recorded by an oscilloscope. The resulting function is deconvoluted to determine the center of the actual ion bunch with an accuracy better than 0.1 ns. For the last part of the 40 μs beam no measurable mass remains in the path of the ion beam. This defines the arrival time of unperturbed ion bunches that corresponds to no energy loss. Therefore, the calculation of the absolute time-of-flight difference and hence the energy loss is possible.

The probe beam frequency can be further improved by shifting the synchronization between the ion bunches and the nhelix laser system. The low shot to shot variations of the nhelix parameters allow us to perform several recordings of the energy loss with identical parameters but with a shifted delay and hence a more detailed measurement of the temporal evolution of the energy loss; in the case of Fig. 2 the timing has been shifted to 2 ns steps with a precision better than 1 ns. In this graph the relative energy loss of four separate experiments on carbon foils with a thickness of 95 μg/cm$^2\pm5\%$ ($\equiv0.5$ μm) is plotted. Within the duration of the laser pulse the whole target is heated to the plasma state. However, only about half of the plasma is ablated into a low-density, hot, and fully ionized corona, which is extended in space over several millimeters; the other part remains in a colder, denser, and only partially ionized state (see Fig. 3 for the corresponding plasma parameters at the end of the heating pulse). At the target thickness used the ion beam passes through enough hot matter, so that changes in the energy loss can be detected with the ToF method with a satisfactory accuracy. Relative values of ΔE are used in Fig. 2 to get rid of the differences in the energy loss due to the variations in the target thickness. 100% corresponds to the energy loss in cold matter of each target. The origin of the x axis is set to 10% of the leading edge of the temporal laser profile averaged over the four separate shots. Note that the error bars only take into account the errors caused within the data analysis; systematic errors like differences in the plasma expansion due to different temporal and spatial laser focus profiles remain unconsidered. With the diamond detector, an energy resolution of the experimental setup of $\Delta E_{kin}/E_{kin}<0.15\%$ is achieved. As soon as the laser hits the target, the experimental data show that the energy loss decreases to a minimum at 3–4 ns. At 9 ns it crosses the level of the cold foil (100% $\approx$ 1.8 MeV) and at 13 ns it reaches its maximum at 130% ($\approx$2.35 MeV). After 20 ns the energy loss starts to decrease due to the three-dimensional character of the plasma expansion.

The exact reason for the first energy-loss decrease has not yet been resolved. However, it has a very similar shape as the inverted temporal laser profile and it is closely related to a broadening of the ion signals as shown in Fig. 2. In fact, this broadening scales very well with the temporal laser profile. Thus, we conclude that there are strong laser-driven inhomogeneities in the target structure. Hence, it is very likely that the energy-loss decrease is related to these inhomogeneities.

Assuming a linear relation between peak broadening and energy-loss decrease, the smoothed sum of the energy-loss values and the accordingly scaled laser intensity profile is also shown in Fig. 2. One possible reason is that there may be optimal detection efficiencies for ions with little angular straggling related to low local integrated mass densities and hence charge states closer to the incident value. Nevertheless, since the focus of this paper is not on target inhomogeneities, the discussion of energy-loss data at times below 12 ns is excluded from this work.

III. THEORETICAL DESCRIPTION OF THE PROJECTILE CHARGE STATE DISTRIBUTION

For any stopping power theory in the intermediate velocity regime the actual charge state of the projectile penetrating the target is of crucial importance. Since it is not possible to measure this parameter for each ion at every location upon its way through the plasma, it has to be determined theoretically. Therefore, a Monte Carlo code describing the charge state evolution of argon ions in cold matter [17] has been extended to describe the plasma case. This code uses the charge-exchange cross-section calculation methods of the ETACHA code [18] for each projectile and target shell. Furthermore, the charge-exchange cross sections for argon ions in ground state in solid carbon have been determined experimentally in [19]. These ground-state cross sections are compared to the results calculated by ETACHA. This comparison leads to a corrective scaling for the results of the theoretical ETACHA calculations and is also used for the cross-section calculations of excited states of Ar in cold matter to improve the MC code's accuracy. To extend its scope of application to the plasma case the calculation methods for the charge-exchange processes have been modified as listed in the following:

(i) The ionization and excitation cross sections in plasma differ from those in cold matter mainly due to the different screening lengths of the target ions. These screening lengths have been calculated using the Hartree-Fock code RCN [20]. The range of the carbon ions potential is limited by the Debye length of the plasma described by a Yukawa potential $V(r)=(Z_T/r)\exp(-\frac{r}{d})$.

(ii) The nonradiative capture is the dominant recombination mechanism in this projectile-target configuration. The target screening and the occupation numbers of the target were adjusted to the local average ionization degree of the plasma.

(iii) For radiative electron capture the Bethe-Salpeter formula is used.

In addition, cross sections for electron-impact ionization [21], dielectronic recombination [22], and three-body recombination [23] have been added to the code.

The plasma parameters are taken from the results of MIMOZA-2D [24] simulations which have been benchmarked with our plasma diagnostics during the experiment, especially with our interferometry measurements (see the Appendix for the full set of plasma parameters). Figure 3 shows the resulting projectile charge state distribution of argon (upper graph) with an incident charge state of 16+ in the plasma target at $t=12$ ns after the beginning of the heating pulse as well as the consequential mean projectile charge state. The calculated plasma parameters—ion density, temperature, and ionization degree—are also shown in this graph. At this time, right at the end of the heating pulse, about half of the carbon plasma is in a low-density fully ionized state; the other half remains only partially ionized ($q\approx 2$–4). Therefore, this time step is convenient to show the effects on the charge state distribution in both the colder partially ionized plasma and the fully ionized part. The ionization of the target merely leads to a slight increase in the projectile ionization and excitation cross sections and balances approximately the decrease due to the lower collision frequency [25]. Therefore, only small deviations in the projectile mean charge state compared to cold matter are observed in the partially ionized part ($\bar{Q}_{solid}=15.6$ and $\bar{Q}_{gas}=15.1$ according to [26]). As soon as the average ionization degree of carbon exceeds the value of 4 the nonradiative recombination cross sections are significantly reduced with further increasing target ionization. This is due to the fact that recombination from the target's K shell is dominant in this projectile-target combination. This leads to considerable changes in the projectile charge state distribution and hence increased projectile mean charge states even compared to the solid state—as can be clearly seen from Fig. 3—with a maximum value of $\bar{Q}_{pl,max}=16.2$ in the hot low-density corona.

IV. THEORETICAL RESULTS ON ENERGY LOSS AND COMPARISON WITH EXPERIMENTAL DATA

The theoretical description of the energy loss was carried out using the CASP code within the "unitary convolution approximation" [5]. A modified version of the code allows the calculation of the energy transfer of a projectile with a defined charge state to the bound electrons of ionized carbon using WKB binding energies [27]. The plasma's charge state distribution is taken into account by solving the Saha equation according to [28]. The mean energy transfer I_{Bethe} for the ionized target has been obtained by a fitting procedure to Hartree-Fock-Slater results. The energy transfer to free electrons is modeled by replacing possible transitions by a single oscillator with an excitation energy equal to the plasmon energy according to the free-electron density. This approach leads to stopping cross sections for argon of a defined charge state for any set of plasma parameters needed. These calculations have been performed for all projectile charge states; the case of $^{18+}$Ar at 4 MeV/u is shown exemplified in Fig. 4. For high temperature and low ion density the stopping cross sections are up to a factor of 2 larger ($S_{cross}=9.5\times 10^{-13}$ eV cm^2) than for high density and low temperature ($S_{cross}=4.5\times 10^{-13}$ eV cm^2) due to the fact that the target is fully ionized and the excitation energy of the plasmons is a lot smaller than that of the bound electrons. These results exceed previous calculations made in [29]. The plateau of the cross section between 20 and 40 eV for moderate to low densities is due to the stable configuration of C^{4+}. Therefore, the main effect on the stopping cross-section results from the ionization of the K-shell electrons of carbon since the difference in the excitation potential is the largest.

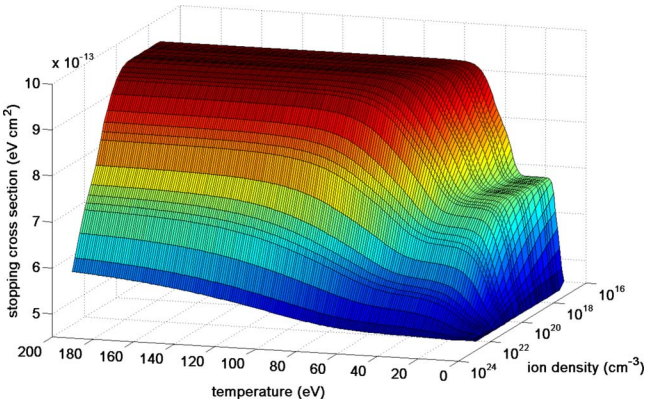

FIG. 4. (Color online) Calculated stopping cross sections for $^{18+}$Ar at 4 MeV/u with fixed charge state in carbon plasma regarding the contributions of bound electrons and free electrons calculated by the CASP code.

The resulting stopping cross sections from the CASP calculations can be combined with the Monte Carlo simulation described above to include the influence of the different projectile charge states in the plasma target. This allows us to determine the stopping power of each projectile at its current charge state at every point in the target. No effective charge description of the projectile is needed in this method. Projectile excitation is neglected in the stopping power calculation. Figure 5 shows the resulting stopping powers (solid blue curve) in the plasma target 12 ns after the beginning of the laser pulse. The contributions of free (dashed red line) and bound (dotted green line) electrons are plotted separately. The plasma parameters can be found in Fig. 3. In the colder part of the plasma both bound and free electrons make a significant contribution to the stopping power in the plasma, although the total stopping power only narrowly exceeds the one in cold matter (dashed-dotted cyan curve). In the fully ionized part however the total stopping power equals the stopping through free electrons and exceeds the one in cold matter by more than a factor of 2.

Integration over the line density delivers the total energy loss of argon in the carbon plasma. The theoretical results are plotted over time in Fig. 6 as well as the experimental data. The plasma parameters used for the calculations can be found in the Appendix. In addition, the energy loss has been calculated with the same code for the same target's density

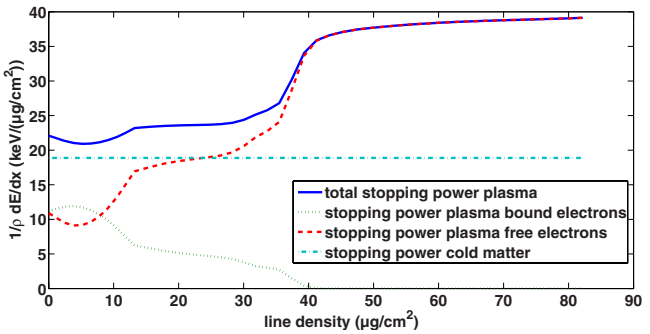

FIG. 5. (Color online) Stopping power 12 ns after the beginning of the laser pulse.

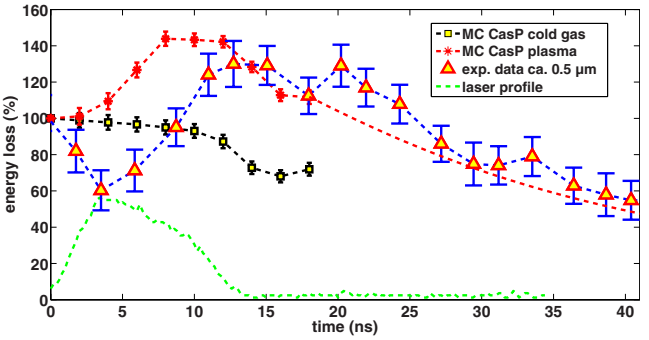

FIG. 6. (Color online) Comparison between experimental and theoretical energy-loss data of argon in carbon plasma. After the end of the laser pulse the energy loss clearly exceeds the one in the cold foil and agrees well with the theoretical calculations.

distributions assumed as an expanding neutral gas (square markers). This allows us to determine the plasma effect on the stopping compared to cold matter. Since projectile charge effects are of minor importance, this curve can be furthermore used to identify the decrease in the average integral mass penetrated by the ion beam. There is a difference between the experimental data and the theoretical calculations for the first 12 ns due to the above discussed inhomogeneities. For the period between 12 and 18 ns after the end of the laser pulse in the experiment, and hence the area of interest in this paper, the agreement between theoretical and experimental data is very good for plasma conditions. For later times no results from the hydrodynamic simulations are available due to numerical problems. To estimate the validity of our model for later times the plasma expansion has been extrapolated using a ballistic expansion of the plasma $[l(x)=\int_0^x \rho(x')dx' \propto 1/[1+(t^2/\tau^2)]$ with $\tau=26.1$ ns obtained from a fit to the two-dimensional (2D) expansion from the hydrodynamic simulations]. The averaged stopping power in the plasma is the same as after 18 ns and assumed to be constant. Note that the error bars of the theoretical calculations only include the straggling due to different individual projectile charge state evolutions within the code. Systematic errors of the calculated charge-exchange and energy-loss cross sections and especially of the hydrodynamic data for the plasma are not included. For times later than 12 ns, the difference between the theoretical values for cold and hot matters is still more than 50%. For these times more than half of the target is fully ionized, which leads to a significantly increased stopping through free electrons since the plasmon excitation energy is much lower than the one of bound electrons, especially compared to the *K*-shell electrons. Moreover, the mean charge state of the projectile in this plasma region is increased as stated above. However, the differences in the excitation energies make 90% of the contribution to the energy-loss increase in the plasma; differences of projectile charge states for the considered projectile-target configuration only make an effect of about 10%.

V. CONCLUSION

In conclusion this paper has presented improved experimental time-of-flight results demonstrating an increased en-

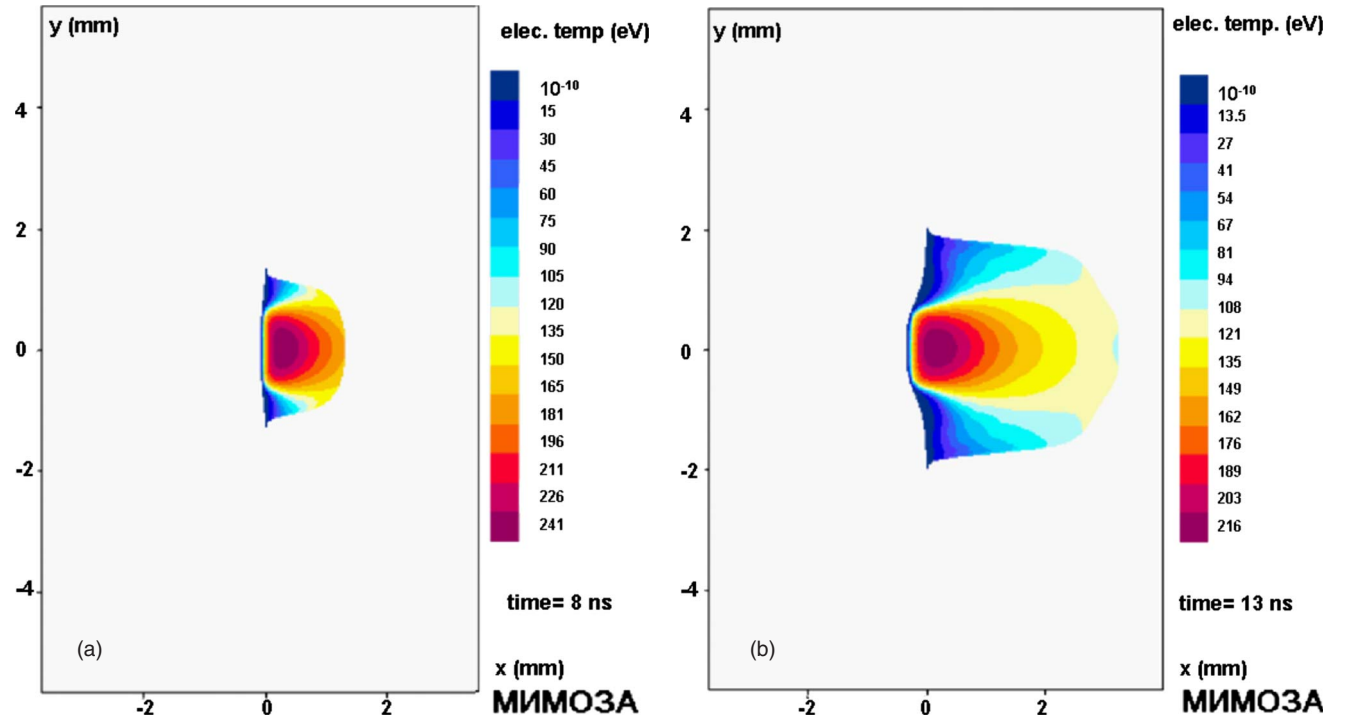

FIG. 7. (Color online) 2D picture of the electron temperature of the carbon plasma calculated by MIMOZA-2D 8 (left) and 13 (right) ns after the beginning of the laser pulse.

ergy loss of argon in laser-generated carbon plasma covering a higher-density and -temperature regime than before. To understand the physical phenomena, a theory for a microscopic description of the energy loss of argon in hot ideal plasma including all relevant projectile charge-exchange and energy-transfer processes has been developed. No effective charge description is used within this scheme. The theoretical calculations agree well with the presented data pointing to the particular importance of the target ionization degree.

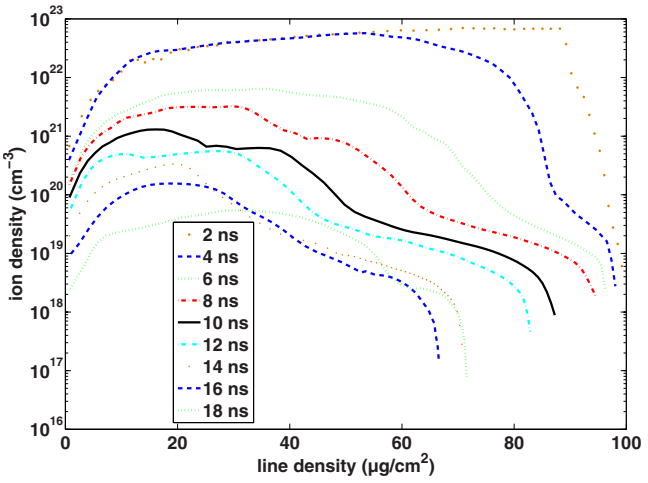

FIG. 8. (Color online) Results of MIMOZA-2D simulations on ion density, which have been used for energy-loss and projectile charge state measurements.

ACKNOWLEDGMENT

This work was supported by ISTC Grant No. 2264.

APPENDIX: HYDRODYNAMIC SIMULATIONS

The MIMOZA-2D simulations have been performed for a laser energy of 50 J at $\lambda = 1.064$ μm with a pulse length of 10 ns (FWHM) and a focus diameter of 1 mm. The temporal laser profile is modeled with 3 ns of linear rise time, 6 ns constant intensity, and 3 ns of linear descent. This corresponds to an average intensity of 5×10^{11} W/cm^2 on the

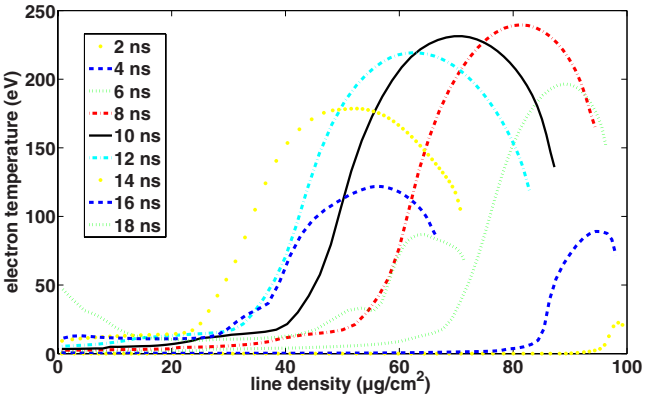

FIG. 9. (Color online) Results of MIMOZA-2D simulations on electron temperature, which have been used for energy-loss and projectile charge state measurements.

target. The simulations have been performed in two dimensions with heat conduction and radiation transport. Reliable results have been obtained until 18 ns after the beginning of the laser pulse, which have been used for this paper. For later times this was not possible due to numerical problems. Two 2D temperature maps at 8 and 13 ns are shown exemplified in Fig. 7. For the projectile charge state and energy-loss calculations the plasma parameters are extracted along the center of the laser beam. The complete set of ion densities and electron temperatures used are shown in Figs. 8 and 9. In these two pictures the decrease in the line density in time can also be seen.

[1] N. Bohr, Philos. Mag. **25**, 10 (1913).
[2] H. Bethe, Ann. Phys. (Leipzig) **397**, 325 (1930).
[3] F. Bloch, Ann. Phys. (Leipzig) **408**, 285 (1933).
[4] P. Sigmund and A. Schinner, Eur. Phys. J. D **12**, 425 (2000).
[5] P. L. Grande and G. Schiwietz, Phys. Rev. A **58**, 3796 (1998).
[6] G. Maynard, G. Zwicknagel, C. Deutsch, and K. Katsonic, Phys. Rev. A **63**, 052903 (2001).
[7] H. Paul, http://www.exphys.uni-linz.ac.at/stopping
[8] M. Tabak *et al.*, Phys. Plasmas **1**, 1626 (1994).
[9] M. Roth *et al.*, Phys. Rev. Lett. **86**, 436 (2001).
[10] K. Weyrich *et al.*, Nucl. Instrum. Methods Phys. Res. A **278**, 52 (1989).
[11] D. Gardes *et al.*, Radiat. Eff. Defects Solids **110**, 49 (1989).
[12] M. Roth *et al.*, EPL **50**, 28 (2000).
[13] D. H. H. Hoffmann *et al.*, Nucl. Instrum. Methods Phys. Res. B **161-163**, 9 (2000).
[14] K. Weyrich *et al.*, Nucl. Instrum. Methods Phys. Res. A **577**, 366 (2007).
[15] G. Schaumann *et al.*, Laser Part. Beams **23**, 503 (2005).
[16] http://www.helmholtz-berlin.de/people/gregor-schiwietz/casp_en.html
[17] A. Blažević, H. G. Bohlen, and W. von Oertzen, Phys. Rev. A **61**, 032901 (2000).
[18] J. P. Rozet *et al.*, Nucl. Instrum. Methods Phys. Res. B **107**, 67 (1996).
[19] A. Blazevic *et al.*, Mat. Fys. Medd. K. Dan. Vidensk. Selsk. **52**, 109 (2006).
[20] R. D. Cowan, *The Theory of Atomic Structure and Spectra* (University of California Press, Berkeley, 1981).
[21] Y. Zhao *et al.*, J. Quant. Spectrosc. Radiat. Transf. **77**, 301 (2003).
[22] K. B. Fournier, M. Cohen, and W. H. Goldstein, Phys. Rev. A **56**, 4715 (1997).
[23] T. Peter, MPQ Report No. 105, 1985 (unpublished).
[24] I. Sofronov *et al.*, *Series Mathematical Modeling of Physical Processes* (2000), Vol. 1, p. 25.
[25] N. Bohr and J. Lindhard, Mat. Fys. Medd. K. Dan. Vidensk. Selsk. **28**, 1 (1954).
[26] G. Schiwietz and P. L. Grande, Nucl. Instrum. Methods Phys. Res. B **175-177**, 125 (2001).
[27] P. P. Szydlik and A. E. Green, Phys. Rev. A **9**, 1885 (1974).
[28] M. R. Zaghloul *et al.*, J. Phys. D: Appl. Phys. **33**, 977 (2000).
[29] G. Maynard, Laser Part. Beams **20**, 467 (2002).